Correspondence to:
D. B. Korovinskiy,
daniil.korovinskiy@oeaw.ac.at

The Inertia-Based Model for Reconstruction of the Electron Diffusion Region

D. B. Korovinskiy[1] [iD], **S. A. Kiehas[1]** [iD], **E. V. Panov[2]** [iD], **V. S. Semenov[3]** [iD], **N. V. Erkaev[4,5]**, **A. V. Divin[3]** [iD], and **I. V. Kubyshkin[3]** [iD]

[1]Space Research Institute, Austrian Academy of Sciences, Graz, Austria, [2]Institute of Physics, Karl-Franz University, Graz, Austria, [3]The Earth Physics Department, Saint Petersburg State University, St. Petersburg, Russia, [4]Institute of Computational Modelling, Siberian Branch of the Russian Academy of Sciences, Krasnoyarsk, Russia, [5]The Applied Mechanics Department, Siberian Federal University, Krasnoyarsk, Russia

Abstract The present study is focused on the problem of reconstruction of the magnetic configuration in the magnetic reconnection electron diffusion region (EDR). The problem is addressed in the frame of electron magnetohydrodynamics with kept electron inertia term. We introduce the new reconstruction model independent of divergence of the electron pressure tensor and reconnection electric field. The model is tested on the magnetotail reconnection event of July 11, 2017 observed by the Magnetospheric Multiscale (MMS) spacecraft in the course of crossing the very core part of the reconnection region, the internal EDR. This new model demonstrates considerably better accuracy of the longitudinal electron velocity reconstruction due to the lower sensitivity to the configuration deviation from the two-dimensional time-independent model adopted in our study. We suggest also a new technique to estimate the guide field, implementing the reconstruction of magnetic potential of the in-plane magnetic field and relying on symmetric properties of magnetic reconnection.

Plain Language Summary Magnetic reconnection is a fundamental plasma process responsible for the magnetic field reconfiguration and transforming magnetic energy to kinetic and thermal energy of plasma. In the Earth's magnetosphere, the magnetospheric conditions are monitored by several spacecraft missions. Among them, the NASA Magnetospheric Multiscale (MMS) mission is designed for exploring the process of reconnection. On July 11, 2017 at about 22:34 UT MMS was located in the magnetotail at a very fortunate position, intersecting the reconnection region in its very central part, the so-called electron diffusion region (EDR).

Since MMS consists of four identical spacecraft, MMS provides an excellent tool for testing analytical models of reconnection. Taking the data of one probe as the boundary condition for the analytical model, one can compare the results of calculations with other probes data. In the present paper we suggest a new model of EDR, and compare it to the existing one using the data of 2017/07/11 event. This comparison has shown that the electron inertia term plays an important role in the EDR physics; the proper handling of this term allows considerable improvement of the EDR reconstruction accuracy.

1. Introduction

Fast magnetic reconnection is an explosive plasma process, bringing the topological reconfiguration of magnetic fields, plasma heating, and acceleration in laboratory and space plasmas (e.g., Gonzalez & Parker, 2016; Yamada et al., 2010). In general, this is a time-dependent multi-scale three-dimensional process (e.g., Bhattacharjee, 2004; Dorfman et al., 2013; Frank, 1999; Xiao et al., 2006), but sometimes reconnection may demonstrate a symmetric configuration and be quasi-stationary. Particularly, at the day side of the Earth's magnetopause, quasi-stationary reconnection has been detected *in-situ* on several occasions (e.g., Gosling et al., 1982; Phan et al., 2004; Retinò et al., 2005) as well as anti-parallel reconnection (Cassak & Fuselier, 2016, and references therein). The latter is more common in the Earth's magnetotail (Paschmann et al., 2013). It is also important that in many cases reconnection can be studied analytically in the frame of two-dimensional models for the considerable length of the reconnection X-line. Configurations with short X-lines demonstrate spreading in the X-line direction (see, e.g., Li et al., 2020, and references therein) in course of time. At last, both at the dayside magnetopause and in the magnetotail (e.g., Cassak &
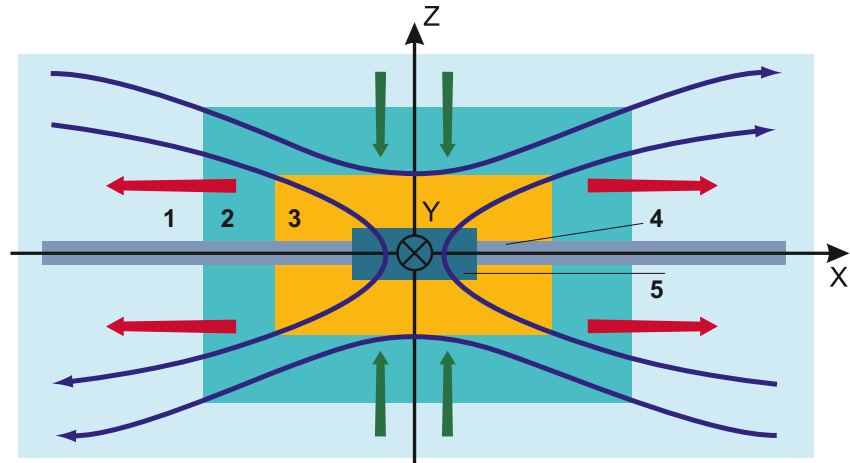
Figure 1. Sketch of the coordinate system *XYZ* and magnetic configuration of the reconnection region. Numbers 1, 2, 3 mark MHD, HMHD, and EMHD domains, respectively, 4 and 5 – external and internal EDR. Blue arrowed curves figure the magnetic field lines. Green and red arrows show the plasma flow directions in the inflow and outflow regions, respectively.

Fuselier, 2016; Hesse & Cassak, 2020), rare particle collisions bring forth the concept of collisionless reconnection (e.g., Birn et al., 2001; Øieroset et al., 2001; Scudder, 2016). Thus, in respect to magnetosheric applications, the simplest analytical framework is provided by the model of fast two-dimensional steady-state collisionless reconnection (Birn et al., 2001), which is adopted in the current paper. To address such a problem, it is convenient to choose the coordinate system shown in Figure 1, where the origin coincides with the X-point (the projection of the reconnection X-line onto the reconnection plane), the x axis is directed along the current sheet (CS), the y axis is directed along the X-line, and the z axis is perpendicular to the CS.

Even in such a simple statement, the problem stays rather complicated for being substantially multi-scaled (e.g., Hesse et al., 2011; Hesse & Winske, 1998; Kuznetsova et al., 2007). Indeed, in ideal magnetohydrodynamics (MHD), magnetic field lines are frozen into the plasma; hence, no topological changes are possible. In non-resistive plasma the Hall effect demagnetizes (Sonnerup, 1979) ions at the scale of the ion inertial length, d_i. Within this so-called ion diffusion region (IDR), the magnetic field stays frozen in the electron fluid. In the interior of this Hall MHD (HMHD) domain, the relation between amplitudes of the ion and electron current densities, $|\mathbf{j}_i| \ll |\mathbf{j}_e|$, allows the neglect of the ion current, yielding the commonly used electron MHD (EMHD) approximation (e.g., Biskamp, 2000; Bulanov et al., 1992; Ji et al., 2014). Approved to be appropriate for plasmas with high and moderate values of the β parameter (Biskamp et al., 1997), where β is the ratio of the gas and magnetic pressures, the condition $|\mathbf{j}_i| \ll |\mathbf{j}_e|$ is found to fulfill not in immediate vicinity of the X-point only, but at bigger distances also, where β drops down to ∼0.1 (Korovinskiy et al., 2020). At last, in the very central part of the reconnection region, the EDR, electrons are also demagnetized due to the electron pressure anisotropy and electron inertia at the scale of the electron inertial length, d_e (e.g., Hesse et al., 2011; Paschmann et al., 2013). EDR, in turn, is splitting in two parts, internal and external (Daughton et al., 2006; Karimabadi et al., 2007; Shay et al., 2007), carrying electron currents in the out-of-plane and longitudinal directions, respectively. The described multi-scaled structure is sketched in Figure 1.

Considering two-dimensional steady-state reconnection and adopting EMHD approximation, the problem is reduced to calculation of the scalar magnetic potential of the in-plane magnetic field, *A* (*x, z*), and evaluation of the out-of-plane magnetic component, $B_y(x, z)$, appearing to be a flux function for the in-plane electron flow. In incompressible plasma with neglected electron inertia equations for *A* and B_y decouple, the former turns to the Grad—Shafranov (GSH) equation (Grad & Rubin, 1958; Shafranov, 1966), and the latter is solved when the solution for *A* is found (Korovinskiy et al., 2008; Sonnerup et al., 2016; Uzdensky & Kulsrud, 2006). In view of the reconstruction problem, one faces here two difficulties, where the first one is pure mathematical and the second one is physical.

The mathematical problem resides in the fact that GSH equation with boundary conditions specified at an unclosed curve (e.g., the satellite trajectory) represents the ill-posed problem; hence, the solution
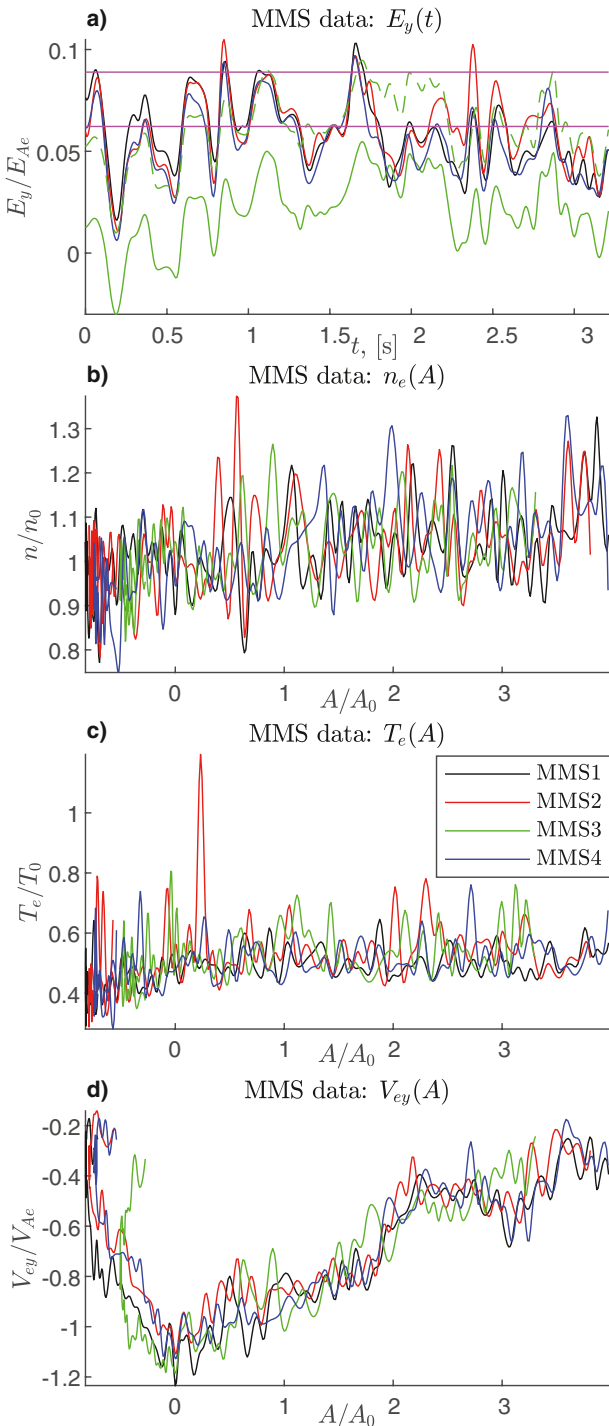
Figure 2. Normalized values of the CS parameters, as measured by MMS probes. Panel (a): electric field E_y versus time, starting from 22:34:01.70 UT. Dashed green curve shows MMS3 data increased for 1.8 mV/m, and horizontal magenta lines draw the values $\varepsilon = \{0.062, 0.089\}$, corresponding to reconnection electric field of $\{2.8, 4.0\}$ mV/m, respectively. Panels (b), (c), and (d) show electron number density n_e, temperature T_e, and velocity V_{ey}, respectively, versus magnetic potential A; at each curve maximum value of A corresponds to the last moment 22:34:04.92 UT of the reconstruction interval. Subscript y marks the M-component in the co-moving frame LMN'. The color code is specified by the legend in panel (c).

is either not unique or not stable, or both. Solution of such problems should imply some regularization procedure, suppressing exponentially growing non-physical oscillations, analogous to those of Hadamard's example (Hadamard, 1923). Two different regularization procedures, suggested by now for this particular problem, are: (a) numerical filtering at each integration step (Sonnerup et al., 2016), and (b) the boundary layer approximation (BLA), neglecting the term $\partial^2 A/\partial x^2$ (Korovinskiy et al., 2008), grounded on the reconnection rate smallness (Cassak et al., 2017; Comisso & Bhattacharjee, 2016) causing the pronounced configuration stretching. The comparison of these two regularization techniques revealed their proximity in terms of the reconstruction accuracy (Korovinskiy et al., 2020). In the current paper we adopt BLA for its relative simplicity.

The physical problem is related to electron kinetic effects, making isotropic fluid approximation inappropriate within EDR. Namely, the out-of-plane magnetic field occurs to be dependent on the out-of-plane component of divergence of the electron pressure tensor, $(\nabla \cdot \hat{P}_e)_y$ (Korovinskiy et al., 2020; Sonnerup et al., 2016). Though some analytical approximations were suggested (Divin et al., 2012, 2016; Hesse et al., 1999), in general, analytical expression for this term is unknown. In view of reconstruction problem, the approximation of Hesse et al. (1999), developed for the case of uniform electron number density, n_e, is the most appropriate. The successful reconstruction of B_y, resting upon this approximation, is performed in several works (Hasegawa et al., 2017, 2019; Sonnerup et al., 2016). The major disadvantage of this approach is the smallness of the applicability domain. Namely, comparing the Hesse et al. (1999) approximation for $(\nabla \cdot \hat{P}_e)_y$ with the genuine value of this term, evaluated by means of particle-in-cell (PIC) simulations, the size of the applicability domain is found to be approximately two times smaller than the size of the number density uniformity region (see Figure 2 in Korovinskiy et al. 2020, and discussion after Equation 53, ibid).

At the same time, the calculation of B_y from the Ohm's law, implying the term $(\nabla \cdot \hat{P}_e)_y$, stays a single option only until electron inertia is neglected. Keeping electron inertia and assuming $n_e = const$, one arrives at the system of two coupled Poisson's equations for A and B_y, which do not contain the term $(\nabla \cdot \hat{P}_e)_y$ (see Equation 12, 13 in Sonnerup et al. (2016) or Equation 51, 52 in Korovinskiy et al. (2020)). In the present paper, we examine the new reconstruction technique, based on the solution of this system, by reconstructing the configuration of EDR, encountered by MMS on July 11, 2017 – an event, reported by Torbert et al. (2018) and considered in a number of studies (e.g., Denton et al., 2021; Egedal et al., 2019; Genestreti et al., 2018; Hasegawa et al., 2019; Nakamura et al., 2019). Namely, we address three reconstruction models, two of which consider the electron inertial term contribution, and the third one, implementing the Hesse et al. (1999) approximation for $(\nabla \cdot \hat{P}_e)_y$, coincides mainly with the model, adopted in Sonnerup et al. (2016) and Hasegawa et al. (2017); Hasegawa et al. (2019) studies. Since the event of 2017/07/11 is well-studied by other authors, we focus on the models comparison rather than on the case study. Alongside with these three models, the new technique for the guide field estimate, relying on the magnetic potential reconstruction, is also discussed.

The paper is organized as follows: in Section 2 we state the reconstruction problem and formulate three reconstruction models, in Section 3 we investigate the current sheet conditions and present the models' functions; reconstruction results are exhibited in Section 4; summary, discussion and conclusions are given in Section 5.

2. The Problem Formulation

We examine the problem of steady magnetic reconnection in collisionless non-resistive compressible plasma in the vicinity of the infinite X-line, at length scale of the electron inertial length. Adopting the reference system, sketched at Figure 1, we assume that for any magnetoplasma quantity U the equality $\partial U / \partial y = 0$ is fulfilled. Considering the plasma, consisting of two particle species, protons and electrons, obeying the quasi-neutrality condition, and adopting an assumption that the proton velocity is negligible as compared to the electron one, we address the reconstruction problem in the frame of single-fluid EMHD, disregarding the problem of the proton motion.

2.1. EMHD Equations

The problem statement includes time-independent equations of the electron fluid motion, Maxwell's equations, and the mass conservation law, which we cast to dimensionless form. Contrary to Korovinskiy et al. (2020), where two-fluid MHD formalism is used, in this paper we use a single-fluid model. Hence, all equations in Section II of Korovinskiy et al. (2020) remain the same, except for the equations of the proton motion and state, which are not considered here. The set of normalization constants is also changed from the proton scale to the electron one: $\{e, m_e, d_e, t^*, B_0, n_0, V_{Ae}, E_{Ae}, p_0, T_0\}$, where e is the elementary charge, m_e is the electron mass; $d_e = c / \omega_e$ is the electron inertial length; c is the speed of light; $\omega_e = \sqrt{n_0 e^2 / (m_e \varepsilon_0)}$ is the electron plasma frequency, where ε_0 is the permittivity of free space; $t^* = \omega_e^{-1}$ is the time scale; magnetic field $B_0 \sim \max |\mathbf{B}|$; electron number density $n_0 \sim <n_e>$; $V_{Ae} = B_0 / \sqrt{\mu_0 n_0 m_e}$ and $E_{Ae} = B_0 V_{Ae}$ are the electron Alfvén velocity and electric field, respectively, where μ_0 is the permeability of free space; $p_0 = B_0^2 / \mu_0$ and $T_0 = p_0 / n_0$ are the normalization constants for pressure and temperature (in energetic units), respectively.

Omitting all details, addressed in Section II of Korovinskiy et al. (2020), where the transition to the electron scale units is performed by the substitution $\mu = 1$, the problem is formulated as follows.

First, Ampère's law reveals that stream function of the in-plane electron flux (nV_{ex}, nV_{ez}) is represented by the out-of-plane magnetic field component $B_y(x, z)$,

$$n\mathbf{V}_{e\perp} = -[\nabla B_y \times \mathbf{e}_y]_\perp, \tag{1}$$

where $\mathbf{e}_y$ is the unit vector of the out-of-plane direction. Here and below, the symbol $\perp$ stands for the in-plane component of any three-dimensional vector.

Second, we introduce the magnetic vector-potential $\mathbf{A} = (0, A(x, z), 0)$ of the in-plane magnetic field, $\mathbf{B}_\perp$, the scalar potential $\varphi(x, z)$ of the in-plane electric field, $\mathbf{E}_\perp$, and effective electric potential, φ^*,

$$\mathbf{B}_\perp = [\nabla A \times \mathbf{e}_y]_\perp, \tag{2}$$

$$\mathbf{E}_\perp = -\nabla_\perp \varphi, \tag{3}$$

$$\varphi^* = \varphi - T_e - \frac{1}{2n^2} | \nabla_\perp B_y |^2 . \tag{4}$$

Since $\mathbf{A}$ has only one non-zero component, in the following we address it as a scalar function. Definition (4) is based on the following model for the electron pressure tensor $(\hat{P}_e)$ divergence, adopted in studies of Sonnerup et al. (2016) and Korovinskiy et al. (2020),

$$\nabla \cdot \hat{P}_e = \nabla_\perp p_e + (\nabla \cdot \hat{P}_e)_y \mathbf{e}_y. \tag{5}$$

The second term in the right-hand side of Equation 5 describes the electron pressure anisotropy, broadening the problem beyond the isotropic fluid approximation, since in a two-dimensional model $\partial p_e / \partial y = 0$, where $p_e = nT_e$ is the scalar electron pressure.

Third, we introduce the notation ε^* for the out-of-plane component of the electron convective electric field,

$$\varepsilon^* = \frac{\varepsilon + (1 / n)(\nabla \cdot \hat{P}_e)_y}{1 - (\partial V_{ey} / \partial A)}, \tag{6}$$

where $\varepsilon = E_y / E_{Ae}$ is the normalized value of the out-of-plane electric field. According to Faraday's law, E_y has to be constant in a steady-state two-dimensional configuration. Under the proper choice of the normalization constants, the reconnection rate is measured as $R_0 = E_y / E_A$ (Schindler, 2007), where $E_A = \sqrt{m_e / m_p} E_{Ae}$.

Magnetic potential obeys Poisson's equation, obtained by substituting (2) to Ampère's law,

$$\Delta_\perp A = nV_{ey}, \tag{7}$$

where $\Delta_\perp$ stands for the in-plane Laplace operator, and the y-component of the Ohm's law is

$$(\mathbf{B}_\perp \cdot \nabla_\perp)B_y = n\varepsilon^*. \tag{8}$$

Using definition (2), Equation 8 takes the form of the Jakobian of the variables transformation $(x, z) \to (A, B_y)$,

$$\left| \frac{\partial(A, B_y)}{\partial(x, z)} \right| = n\varepsilon^*. \tag{9}$$

Since ε^* may turn to zero or infinity at the manifold of measure zero only (according to Equation 6), outside that manifold the quantities A and B_y may be considered as a pair of independent variables, specifying the new coordinate system. The partial derivatives on A and B_y are expressed as follows,

$$\frac{\partial}{\partial A} = \frac{1}{\varepsilon^*}(\mathbf{V}_{e\perp} \cdot \nabla_\perp), \tag{10}$$

$$\frac{\partial}{\partial B_y} = \frac{1}{n\varepsilon^*}(\mathbf{B}_\perp \cdot \nabla_\perp). \tag{11}$$

With Equation 10 and 11, the in-plane component of the Ohm's law (which is nothing else but the equation of motion for electrons) yields two equations for the effective electric potential,

$$\frac{\partial \varphi^*}{\partial A} = V_{ey} + T_e \frac{\partial}{\partial A}\ln(n), \tag{12}$$

$$\frac{\partial \varphi^*}{\partial B_y} = \frac{1}{n}B_y + T_e \frac{\partial}{\partial B_y}\ln(n) + R(A, B_y), \tag{13}$$

where we introduce the notation

$$R(A, B_y) = \frac{1}{n^2}\Big[(\nabla_\perp \ln(n) \cdot \nabla_\perp B_y) - \Delta_\perp B_y\Big]. \tag{14}$$

The quantity R describes the contribution of the electron inertia, since with Equations 1 and 9 it is rearranged as

$$R = \frac{1}{n\varepsilon_*} \mathbf{B}_\perp \cdot \left[(\mathbf{V}_{e\perp} \cdot \nabla_\perp) \mathbf{V}_{e\perp} - \nabla_\perp (V_{e\perp}^2 / 2) \right]. \tag{15}$$

Representation (15) shows that the electron pressure anisotropy is also contributing to the quantity R via the term ε^*.

2.2. Reconstruction Models

Assuming uniform number density, differentiating (12) for B_y and (13) for A, and equating the results, we derive

$$\frac{\partial V_{ey}}{\partial B_y} = \frac{\partial R}{\partial A} = -\frac{1}{n^2} \frac{\partial Q}{\partial A}, \tag{16}$$

where we introduce the notation $Q(A, B_y) = \Delta_\perp B_y$. The reconstruction implies the solution of system (7, 8) or (7, 16) with boundary conditions (BC) specified at a single unclosed curve (satellite trajectory). In the current paper we consider three models for the given problem.

Model 1. Under the assumption $V_{ey} = V_{ey}(A)$, Equation 16 yields $Q = Q(B_y)$. Hence we arrive at two GSH equations:

$$\Delta_\perp A = n V_{ey}(A), \tag{17}$$

$$\Delta_\perp B_y = Q(B_y). \tag{18}$$

According to Equation 15, neglect of the inertial term in the equation of electron motion corresponds to the formal substitution $Q = 0$. We use the term "formal" because the contribution of the inertial term is found to be non-vanishing both in PIC-simulations data (Korovinskiy et al., 2020) and in *in-situ* data set studied here. Electron inertia was neglected in a number of previous studies, such as (Hasegawa et al., 2017, 2019; Korovinskiy et al., 2008, 2011, 2020; Semenov et al., 2009; Sonnerup et al., 2016; Uzdensky & Kulsrud, 2006). However, Equation 18 with zero right part (i.e., the Laplace equation) has not been applied for calculation of B_y.

Model 2. In this model, we release the condition $V_{ey} = V_{ey}(A)$ and consider the Taylor series for $V_{ey}(A, B_y)$ on B_y. Assuming symmetrical configuration, the symmetry conditions require V_{ey} to be even function on B_y. Hence we have $V_{ey} = v_0(A) + 0.5 f(A) B_y^2 + \ldots$. When symmetry is corrupted for any reason, the odd terms contribute to the Taylor series as well. For example, when guide field (the uniform part of the out-of-plane magnetic field) is non-zero, the out-of-plane magnetic field can be written as

$$B_y = B_g + \tilde{B}_y(x, z), \tag{19}$$

where B_g is the guide field, and $\tilde{B}_y$ is the non-uniform Hall magnetic field. Assuming the pronounced asymmetry (B_g is large as compared to $\tilde{B}_y$), we omit all terms of the Taylor series except for the two first ones,

$$V_{ey} \approx V_0(A) + F(A)\tilde{B}_y, \tag{20}$$

where $V_0(A) = v_0(A) + 0.5 B_g^2 f(A)$ and $F(A) = B_g f(A)$. Substituting this linear approximation for V_{ey} to Equation 16 and integrating on A, we derive the representation for $Q(A, \tilde{B}_y) = q_1(A) + q_2(\tilde{B}_y)$, where $q_1 = -n^2 \int F dA$ and $q_2(\tilde{B}_y)$ is an arbitrary function (the constant of integration). Model 1 corresponds to the case $|q_2| \gg |q_1|$. In Model 2 we adopt the opposite assumption. By neglecting $q_2(\tilde{B}_y)$, we arrive at the system of two Poisson's equations,

$$\Delta_\perp A = n V_0(A) - \frac{1}{n} \frac{dQ}{dA} \tilde{B}_y, \tag{21}$$

$$\Delta_\perp \tilde{B}_y = Q(A). \tag{22}$$

Remind that system (21, 22) is applied only for those configurations, where the symmetry of B_y is significantly corrupted. Evidently, the sign tilde in the left-hand side of Equation 22 may be omitted. In the following we omit tilde any time when it is not confusing.

Model 3. The third approach addresses system (7, 8) in the same manner, as it was made in studies of Sonnerup et al. (2016) and Hasegawa et al. (2017); Hasegawa et al. (2019), with two minor modifications. Namely, we make use of the Hesse et al. (1999) approximation for the term $(\nabla \cdot \hat{P}_e)_y$. In normalized units ($m_e = 1$, $e = 1$) it reads

$$-\frac{1}{n}(\nabla \cdot \hat{P}_e)_y = \sqrt{\frac{T_e}{2}}\left(\frac{\partial V_{ex}}{\partial x} - \frac{\partial V_{ez}}{\partial z}\right) = \frac{\sqrt{2T_e}}{n}\frac{\partial^2 B_y}{\partial x \partial z}. \tag{23}$$

Substituting (23) to (6) and (6) to (8) we derive the equation for B_y,

$$\frac{\partial^2 B_y}{\partial x \partial z} = \frac{1}{\sqrt{2T_e}}\left\{\left(1 - \frac{\partial V_{ey}}{\partial A}\right)\left[\frac{\partial B_y}{\partial x}\frac{\partial A}{\partial z} - \frac{\partial B_y}{\partial z}\frac{\partial A}{\partial x}\right] + n\varepsilon\right\}, \tag{24}$$

where the term $\partial V_{ey}/\partial A$ is responsible for the electron inertia (see Equation 10). Without this term, Equation 24 is solved in (Hasegawa et al., 2017, 2019; Sonnerup et al., 2016) with $T_e = const$. In our study, Equation 24 is addressed under the assumption $T_e = T_e(A)$. The system is closed by the GSH Equation 17 for A.

Thus, Model 1 and 3 are stated by two decoupled equations, where Equation 17 for A is the same; in Model 2 equations for A and B_y are coupled, where the former attains small (as we will see below) extra term. Equations for B_y, at contrary, are substantially different in all three models. In Model 3 B_y is calculated from the Ohm's law with using approximation (23), neglecting electron inertia, and relying on the linear approximation for the $\hat{P}_e$ components (Kuznetsova et al., 1998) and the assumption of the nongyrotropic electric field constancy inside EDR (Kuznetsova et al., 2000). Models 1 and 2 address the Ohm's law without extra simplifying assumptions (except for the assumption $n = const$ common for all three models), differing from each other in the specific type of V_{ey}, handled as a function of one ($V_{ey}(A)$ in Model 1) or two ($V_{ey}(A, B_y)$ in Model 2) variables.

3. Reconstruction Setup

### 3.1. CS Condition and the Models' Functions

We consider magnetotail reconnection event, seen by MMS3 spacecraft on July 11, 2017 at around 22:34 UT (Torbert et al., 2018), and studied in the paper of Hasegawa et al. (2019), providing us a reference point. The orbit of MMS3, located at $(-21.6, 4.2, 3.6)\,R_E$, where R_E stands for the Earth radius, in geocentric solar ecliptic coordinate system (GSE), can be found in Figure 1**J** of Torbert et al. (2018), and event overview is presented in Figure 1 of Hasegawa et al. (2019). We initiate the reconstruction procedure by implementing the results derived by Hasegawa et al. (2019). Namely, satellite data are transformed to the same optimized LMN coordinate system with $\mathbf{e}_L = (0.9605, -0.1735, -0.2177)$, $\mathbf{e}_M = (0.0985, 0.9432, -0.3272)$, $\mathbf{e}_N = (0.2604, 0.2832, 0.9230)$ in GSE, after that all plasma quantities are recalculated to the system LMN', moving with the velocity $\mathbf{V}_0 = (-231.70, -176.75, -59.20)\,km/s$ as respect to LMN, estimated as the structure velocity in Hasegawa et al. (2019). Magnetic configuration is reconstructed with boundary conditions specified by MMS3 data (except for the boundary condition for function Q, specified by an averaged value, defined below). The reconstruction time interval is extended from 22:34:01.70–22:34:03.10 UT in Hasegawa et al. (2019) to 22:34:01.70–22:34:04.92 in this paper. All computations are performed in normalized units. Apart from the electron charge and mass, the set of normalization constants includes $B_0 = 3\,nT$ and $n_0 = 0.035\,cm^{-3}$. Other constants, constrained by B_0 and n_0, are $d_e = 28.4\,km$, $A_0 = 85.2\,nT \cdot km$, $T_0 = 1.28\,keV$, $V_{Ae} = 15 \cdot 10^3\,km/s$, $E_{Ae} = 45\,mV/m$, $p_0 = 7.16\,pPa$, and $t^* = 1.9\,ms$. The normalization constants for number density and magnetic field are chosen for $n \approx 1$ and $\max|V_{ey}| \sim 1$ in normalized units.
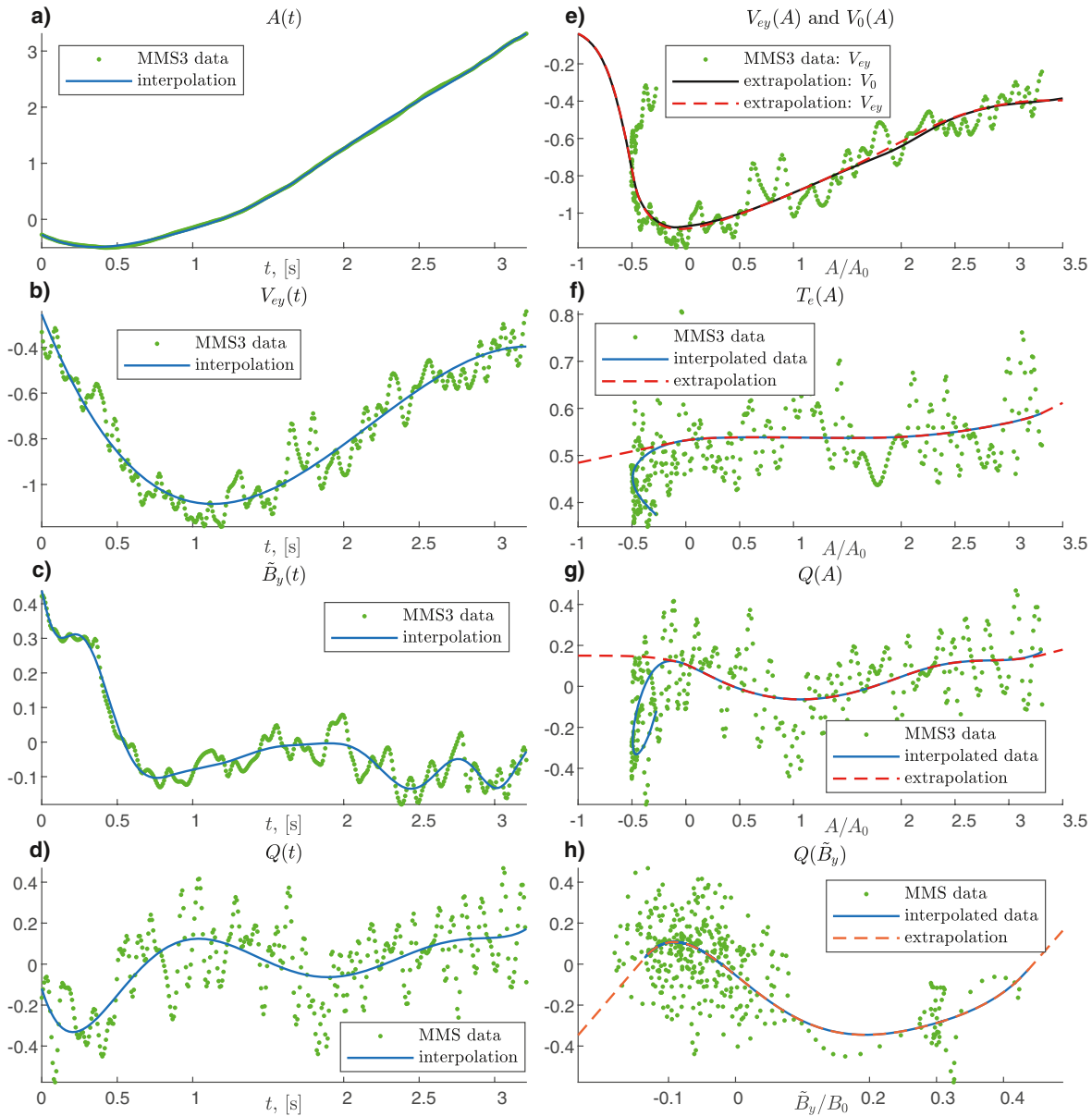
Figure 3. The functions, utilized by reconstruction models (in LMN'): measured (green, dotted), interpolated (blue, solid) and extrapolated (red, dashed) values. In the left column, magnetic potential A, V_{ey}, $\tilde{B}_y$ and $Q = \Delta_\perp B_y$ are plotted versus time in panels (a)–(d), respectively. Right column depicts $V_{ey}(A)$, $T_e(A)$, $Q(A)$ and $Q(\tilde{B}_y)$ in panels (e)–(h), respectively. Black solid curve in panel (e) shows extrapolated function $V_0(A)$ of Equation 20.

The applicability of the general approach of our study is characterized by the CS conditions, presented in Figure 2, where normalized values of the out-of-plane electric field, electron number density, temperature, and out-of-plane velocity, registered by four MMS probes, are plotted. E_y is plotted versus time, measured from the initial moment $t_0 = 22:34:01.70$ UT. Other quantities are plotted versus magnetic potential, calculated in the co-moving frame LMN' at each spacecraft trajectory S_k as $A_k(S_k) = \int_{S_k} (B_z dx - B_x dz) + a_k$, where k is the spacecraft number, and integration constant a_k is chosen to provide a peak value of $V_{ey,k}(A_k)$ at $A_k = 0$. For simplicity, here and below we denote longitudinal components by x, out-of-plane components by y, and normal components by z. In Figure 2 and throughout the paper, the MMS data and corresponding reconstruction results are shown by black color for MMS1, by red for MMS2, by green for MMS3, and by blue for MMS4.
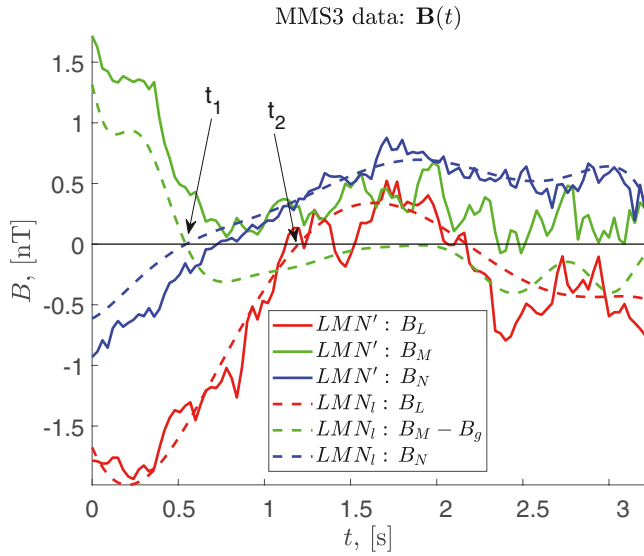
Figure 4. Solid curves: magnetic field components as observed by MMS3, transformed to co-moving frame LMN'. Dashed curves: polynomial fit of magnetic field components in rotated system LMN_l, where B_M component is reduced for the guide field value. Time moments t_1 and t_2 mark the MMS3 crossings of the N and L axis, respectively, in LMN_l coordinate system.
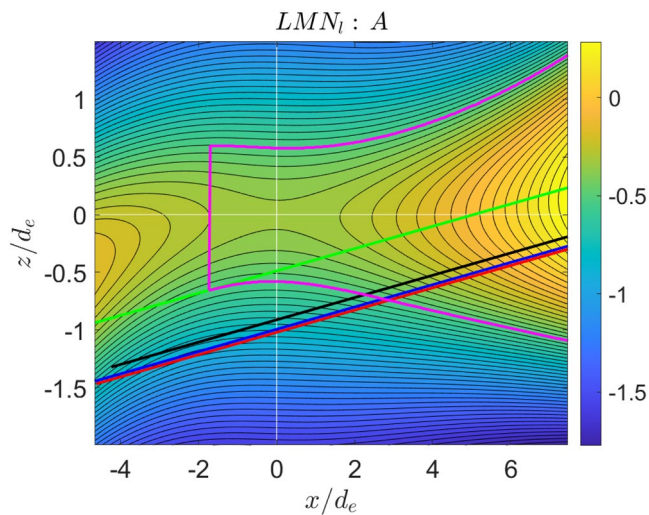

Figure 5. Magnetic potential: reconstruction in coordinate system LMN_l by Equation 17. White lines plot the axes, and oblique colored lines plot the trajectories of MMS probes {1, 2, 3, 4} by {black, red, green, blue} colors, respectively. BC: MMS3. Magenta curve bounds the region where magnetic potential stays within the interval specified by the boundary conditions and function $V_{ey}(A)$ is well-defined (see Figure 3e). For better visibility of the X-point vicinity, the demonstrated reconstruction interval is reduced to 1.46 s.

Figure 2a shows that the condition $E_y = const$ is approximately fulfilled at the loci of all MMS probes, except for MMS3. The value of E_y as observed by MMS3 exhibits an offset of about -1.8 mV/m (see green dashed curve in Figure 2a plotting the value of E_y with the corrected offset). In addition to this offset, E_y demonstrates significant oscillations at all MMS spacecraft, so that the condition $E_y = const$ is fulfilled with an accuracy not exceeding 30%. It means that the configuration is not exactly two-dimensional or non-stationary, or both. The offset of E_y value observed by MMS3 implies also that the M axis of the coordinate system LMN' does not exactly match the direction of the X-line (Genestreti et al., 2018). Hence, E_y is contributed by the Hall electric field (e.g., Drake et al., 2008).

Figures 2b and 2c demonstrate that the condition $n_e = const$ is fulfilled to high accuracy (the linear regression coefficient is ≈ 0.03), and the electron temperature is mainly supporting the assumption $T_e = T_e(A)$. Since the pair $\{A, B_y\}$ compose the system of independent variables, non-identity of the profiles of any magnetoplasma quantity $U(A)$, evaluated by different probes' data, indicates the dependence of this quantity on the second variable, B_y. Particularly, according to Figure 2d, the out-of-plane velocity demonstrates the behavior, which can be described by the model equation $V_{ey} = V_0(A) + \delta$, where V_0 is the main term and δ is some small, but non-vanishing extra term that depends on B_y (and, perhaps, on A). Despite the confusing oscillations, the contribution of this term is clearly recognized by comparison of the red and green curves, demonstrating the inversion of local minima and maxima at $A \approx \{0.4, 1.8, 3\}$. It is seen also that close to the left boundary of the figure (the initial period), two-valued function $V_{ey}(A)$ is detected at all probes, which goes beyond the model concept.

The models' functions are shown in Figure 3, where measured values are plotted by green dots, polynomial interpolations are plotted in blue, and extrapolated functions, used for reconstruction, are plotted by red color (except for $V_0(A)$ shown by black curve in the top right panel). The function $Q = \Delta_\perp B_y = n \left(\partial V_{ex}/\partial z - \partial V_{ez}/\partial x\right)$ is estimated as $\Sigma Q_{3k}/3$, where $k = \{1, 2, 4\}$ and Q_{3k} is calculated by data of the third and k-th spacecraft. All other boundary values are provided by MMS3 data. The number density is calculated as zero order polynomial fit of n_e, $n = 1.016$. Panels (c) and (h) of Figure 3 show $\tilde{B}_y(t)$ and $Q(\tilde{B}_y)$, respectively, where $\tilde{B}_y$ of Equation 19 is evaluated with guide field $B_g = 0.45$ nT (see below).

It is seen (Figure 3a) that at $t \approx 0.43$ s magnetic potential exhibits minimum value ≈ -0.5, at smaller values of t the function $V_{ey}(A)$ (Figure 3e) switches to another branch, which cannot be used in reconstruction. This means that accurate reconstruction results in the region, where $A < -0.5$, are not expected, because the choice of extrapolating function for V_{ey} is rather arbitrary. The same holds for functions $T_e(A)$ and $Q(A)$, shown in Figures 3f and 3g, respectively. For $A > -0.5$ all functions on A, shown in panels (e)–(g) by green dots, are relatively well-defined functions. On the contrary, values of $Q(\tilde{B}_y)$, shown by green dots in Figure 3h, demonstrate nearly chaotic behavior in the major part of the reconstruction interval (see for the cloud of green dots located at $\tilde{B}_y \sim -0.1$, corresponding to interval $t > 0.5$ in Figure 3c. Comparing well-defined function $Q(A)$ in Figure 3g with the ill-defined function $Q(\tilde{B}_y)$ in Figure 3h, one can presume the reconstruction Model 2 to be more relevant to the EDR conditions than Model 1.
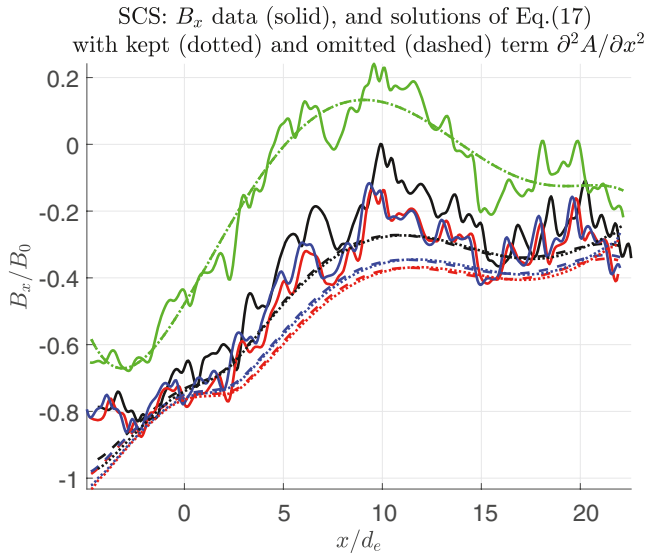
Figure 6. Comparison of two regularization techniques for Equation 17 in SCS: observed values of B_x (solid curves) as compared to the solutions of Equation 17 with kept (dotted curves) and omitted (dashed curves) term $\partial^2 A/\partial x^2$. The color code is the same to the one of Figure 2. BC: MMS3.

Note that none of the quantities, plotted in Figure 3, change after coordinate rotation in the reconnection plane.

3.2. The Guide Field Estimate

In BLA the accuracy of reconstruction is sensitive to orientation of the coordinate system with respect to CS. If one neglects the term $\partial^2/\partial x^2$ in the Laplace operator, the minimal error is achieved, when the x axis coincides with the direction of minimal variations of the magnetoplasma quantities, and the z axis – with the direction of maximal variations. Hence, the optimal coordinate system has to be a local LMN system. Identification of this optimal coordinate system may be gained by performing reconstruction of the magnetic potential in LMN' and estimating the value of the required rotation angle. However, the particular event considered here demonstrates a remarkable peculiarity. Namely, looking at Figure 4a of Hasegawa et al. (2019), one notices that MMS3 trajectory crosses EDR in the very close vicinity of the X-point, where the magnetic configuration is nearly symmetrical both in longitudinal and in the cross-structure directions. This gives us an opportunity for accurate evaluation of the required rotation angle and the guide field value, relying on these symmetry properties.

In the symmetric configuration both the normal and the out-of-plane components of the magnetic field change sign at the vertical axis. Solid curves in Figure 4 plot the magnetic field components observed by MMS3 rotated to co-moving frame LMN' versus time. It is seen that at those moments when B_L and B_N components change signs, the B_M component does not. Since in-plane magnetic configuration is nearly symmetrical (in the vicinity of the X-point), this means that the guide field is nonzero. Applying the substitution (19), we require that in local coordinate system, denoted as LMN_l, the components B_N and $\tilde{B}_M$ change sign at the same moment t_1, corresponding to the spacecraft crossing of the N axis of LMN_l. Apparently, the value of t_1 depends on the selected value of B_g. This requirement gives the orientation of LMN_l, because the rotation angle θ: $LMN' \rightarrow LMN_l$ is evaluated in LMN' as arctan $[B_N(t_1)/B_L(t_1)]$.

Thus, by fixing some value of B_g we specify the moment t_1 of crossing the N axis in LMN_l. Then, the rotation angle is evaluated and all in-plane components are transformed to this system (see dashed curves in Figure 4). Due to the symmetry, the moment t_2, when the longitudinal component B_L changes sign, corresponds to the crossing of the L axis in LMN_l. Thus, LMN_l is fully defined. Solving Equation 17 in LMN_l, we evaluate the magnetic potential and in-plane magnetic components. The symmetry condition requires in-plane magnetic field to vanish at the coordinates origin, therefore the value of B_g is found by means of minimization of B_L and B_N in the origin. Taking into account the guide field estimate of 0.3–0.5 nT from Genestreti et al. (2018) and 0.4 nT from Torbert et al. (2018), we initiated the described procedure by setting the value of the guide field to 0.4 nT. The minimum value of the in-plane magnetic field is achieved for $B_g = 0.445 \pm 0.005$ nT, yielding $B_L(0) = 1.5 \cdot 10^{-4}$ nT and $B_N(0) = -0.0011$ nT ($5 \cdot 10^{-5}$ and $-3.8 \cdot 10^{-4}$, respectively, in normalized units). Since such precision of the guide field estimate is completely unnecessary (for instance, the accuracy of the method may be reduced by non-ideal CS symmetry), we rounded up the value of B_g to 0.45 nT ($0.15B_0$). The corresponding solution for magnetic potential, obtained in LMN_l coordinate system, is shown in Figure 5. The rotation angle θ amounted to 8.58° in anti-clockwise direction.

3.3. Key Factors Affecting the Reconstruction Performance: Coordinate System, BLA, Extrapolation of $V_{ey}(A)$
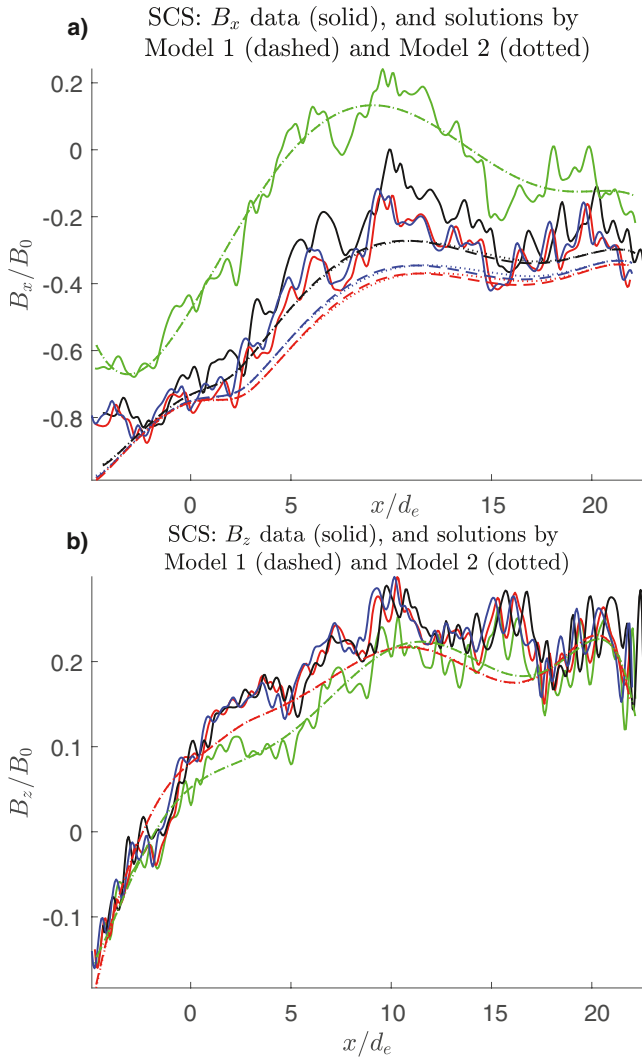
Though the coordinate system LMN_l provides the best performance of BLA, the oblique trajectory does not allow evaluation of the derivative $\partial/\partial x$, needed in Equation 24. Meanwhile, the inclination of the probes' trajectories with respect to the horizontal axis amounts to 14.37° in LMN', and 5.79° only in LMN_l. Therefore, we pass from LMN_l to the "satellite coordinate system" (SCS), where probes' trajectories are parallel

Figure 7. Reconstruction in SCS. Top: B_x, bottom: B_z. Observed values (solid) as compared to the reconstruction prediction, evaluated by Equation 17 (dashed) and Equation 21 (dotted). The color code is the same to the one of Figure 2. BC: MMS3. For better visibility, in bottom panel reconstruction results for MMS1 and MMS4 are not shown.

to the x axis. Even though the rotation angle $LMN_l \rightarrow$ SCS is small, SCS is not optimal for BLA, hence the contribution of the term $\partial^2 A/\partial x^2$ in Equation 17 is to be estimated. To this end, Equation 17 is solved in SCS with and without this term. The solution with kept derivative implies the problem regularization by means of the numerical smoothing at each integration step, as it was suggested in study of Sonnerup et al. (2016). As for the solution of Equation 17 with omitted term $\partial^2 A/\partial x^2$ (i.e., solution in BLA), BLA is the regularization procedure itself. The detailed comparison of these two regularization techniques is provided in Korovinskiy et al. (2020). Two solutions of Equation 17 are compared to each other and to the *in-situ* data in terms of the B_x value in Figure 6. Comparing the dashed and dotted curves in this figure, we see that the contribution of the term $\partial^2 A/\partial x^2$ is negligible. Moreover, the solution derived in BLA demonstrates a slightly better accuracy. Therefore, in the following all equations containing the Laplace operator are solved in BLA.

In the major part of the reconstruction region ($x > -2.5$) the reconstructed values demonstrate good qualitative and quantitative agreement with the data, exhibiting some systematic error for about 20% downgrade, which characterizes the deviation of the real CS conditions from the model assumptions. In the leftmost part of the CS ($x < -2.5$) the reconstruction fails. Note that the magnetic potential at the MMS3 trajectory reaches a minimum value at $x = -1.8$ (the leftmost coordinate of the magenta curve in Figure 5 recalculated from LMN_l to SCS); to the left of this point the function $V_{ey}(A)$ switches to another branch, while we are switching (some time earlier) from the well-defined function to its extrapolation (see Figure 3e). Besides that, out-of-plane electric field E_y, as observed by MMS3, is considerably suppressed there, attaining even negative values (see Figure 2a). Apparently, the two-dimensional steady-state reconnection model does not suite real CS conditions in the region $x < -2.5$.

Note that by varying the function, extrapolating $V_{ey}(A)$ to the left, one could improve the accuracy of reconstruction for B_x in the leftmost part of the box. However, it is achieved at the expense of considerable reduction of the B_y reconstruction accuracy. Also, the trajectories of all other probes, except for MMS3, leave the trusted reconstruction region (contoured by magenta curve in Figure 5) much further than MMS3, at $x = 2.1$ for MMS1, 2.6 for MMS4, and 2.8 for MMS2. Meanwhile, within the interval $x \in (-2.5, +2.8)$ we observe good quality of the reconstruction. It means that at least the initial part of our extrapolating function for $V_{ey}(A)$ is correct.

4. Reconstruction Results

4.1. Comparison of Model 1 with Model 2

We start the comparison of Models 1 and 2 from exploring the in-plane magnetic field reconstruction accuracy, that is, we compare the solutions of GSH (17) and Poisson's (21) equations. Note that Equation 17, adopted by Models 1 and 3, does not depend on B_y, while in Model 2 coupled Equations (21 and 22) are solved.

Figure 7 presents the solutions for B_x and B_z as derived from the GSH and Poisson's equations at the MMS spacecraft trajectories, along with the measured values. Solutions for B_z demonstrate no recognizable difference. Solutions for B_x do not differ at $x < 5$, in the interval $5 < x < 12$ solution of GSH equation exhibits minor advantage, at $x > 12$ solution of Poisson's equation reveals a slightly better accuracy. In fact, at such
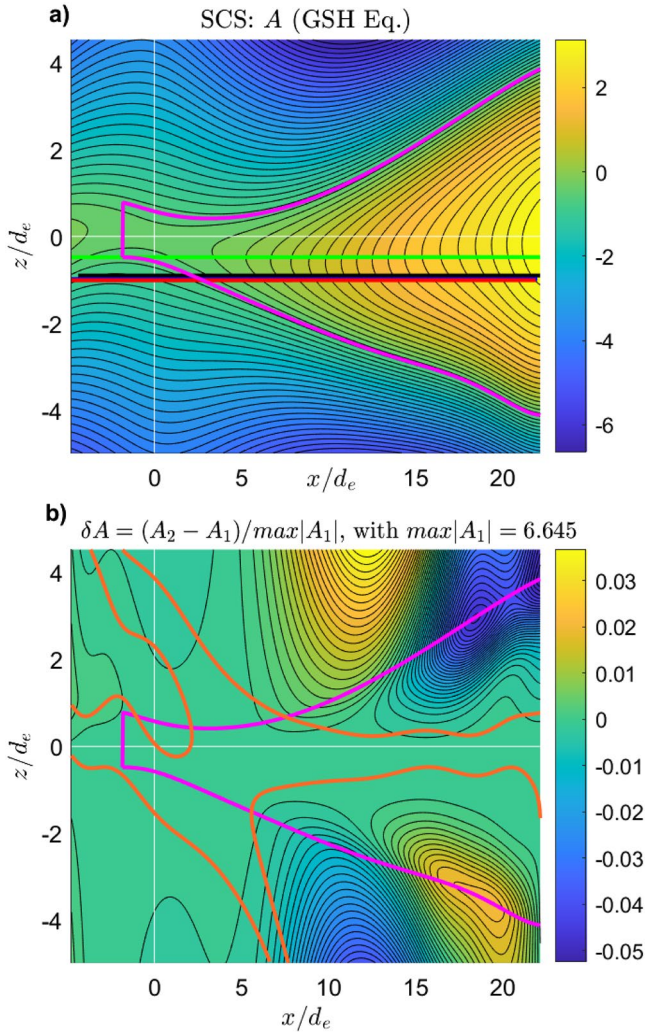
Figure 8. Reconstruction in SCS. Top: A (x, z) as obtained from solution of Equation 17. Bottom: $\delta A = (A_2 - A_1)/max|A_1|$, where A_1 is the solution of Equation 17, and A_2 is the solution of Equation 21. White lines plot the axes, magenta curve bounds the region where magnetic potential stays within the interval specified by the boundary conditions and function $V_{ey}(A)$ is well-defined (see Figure 3e). Horizontal colored lines in top panel plot the trajectories of MMS probes (color code is the same to the one of Figure 5), and orange curves in bottom panel contour region, where B_y stays within the interval specified by BC (see Figure 3c).

small distances (maximum spacecraft separation amounted 0.63 d_e between MMS3 and MMS2), Models 1 and 2 provide the same solutions for magnetic potential and its derivatives.

Solutions at large distances are compared in Figure 8, where top panel plots the solution of Equation 17. Visually, solution of Equation 21 looks nearly identical (not shown), the difference of these two solutions is drawn in the bottom panel of Figure 8, depicting the quantity $\delta A = (A_2 - A_1)/max|A_1|$, where A_1 is the solution of Equation 17, and A_2 is the solution of Equation 21. It is seen that this normalized discrepancy does not exceed the value of 5%. The peaking values of δA are reached in those regions, where values of B_y (contributing the second term in the right-hand side of Equation 21) go far beyond the interval, specified by BC.

The solutions for $\tilde{B}_y$ and V_{ex} as derived from the GSH (18) and Poisson's (22) equations at the MMS spacecraft trajectories are compared to each other and to measured values in Figure 9. In the left part of the reconstruction region, $-2.3 < x < 13$, and in the rightmost spot $x > 22$ both solutions for $\tilde{B}_y$ exhibit good agreement with the data. In the right part, $13 < x < 22$, the solution of Poisson's equation is still accurate, while the GSH equation solution demonstrates the lower accuracy, where the reconstruction error is increasing with the distance from the boundary. At $x < -2.3$, on the contrary, Model 1 appears somewhat better than Model 2. Solutions for V_{ex} show the same features, except for the leftmost part of the sheet where reconstruction by Model 1 fails in the region $x < 1$, while the Model 2 reconstruction is collapsing at $x < -1$ only.

Thus, even at such small distances Model 2 demonstrates evident advantage over the Model 1. This is confirmed by two-dimensional plots of reconstructed $\tilde{B}_y$ values shown in Figure 10. It is seen that in Model 1 | $\tilde{B}_y$ | is growing extremely fast, reaching the value of 6 B_0 at 2 d_e from the MMS3 trajectory (at this distance, the peaking values of B_x and B_z are about 2 and 0.4, respectively). Of course, this result may be corrected by different choice of the extrapolating function $Q(\tilde{B}_y)$. Particularly, the blue curve of Figure 3h demonstrates a quasi-periodic behavior with the quasi-period of about 0.6 B_0. However, extrapolating this curve in the same quasi-periodic manner, the problem 18 turns to the equation $\Delta_\perp \tilde{B}_y \sim \sin(2\pi \tilde{B}_y / 0.6)$. Applying BLA, we finally arrive at the non-linear pendulum equation, yielding an oscillating (on z) solution, which is unphysical for EDR.

Keeping in mind the results of this section and taking into consideration the absence of any prominent dependence of $Q(\tilde{B}_y)$ in the most part of the CS (cloud of green points in Figure 3h corresponds to the interval

$t > 0.5$ in Figure 3c), Model 1 shows worse consistency with observations than Model 2. Good agreement of the solutions for $\tilde{B}_y$, obtained from Model 1 and Model 2, is observed in the regions, where small values of the function Q make both GSH and Poisson's equations for $\tilde{B}_y$ performing similar to the Laplace equation, showing minor discrepancy of the solutions at small distance of $|z| \lesssim 0.6$ d_e (from the boundary). On the same reason, solutions for A, derived by using these two models, are nearly identical at these small distances, as like as the stagnation points positions, plotted by red asterisks in Figure 10. Both models reveal the earthward shift of the stagnation point for about 110 km from the X-point (in LMN'), which is somewhat larger than the value of 90 km obtained by Hasegawa et al. (2019).
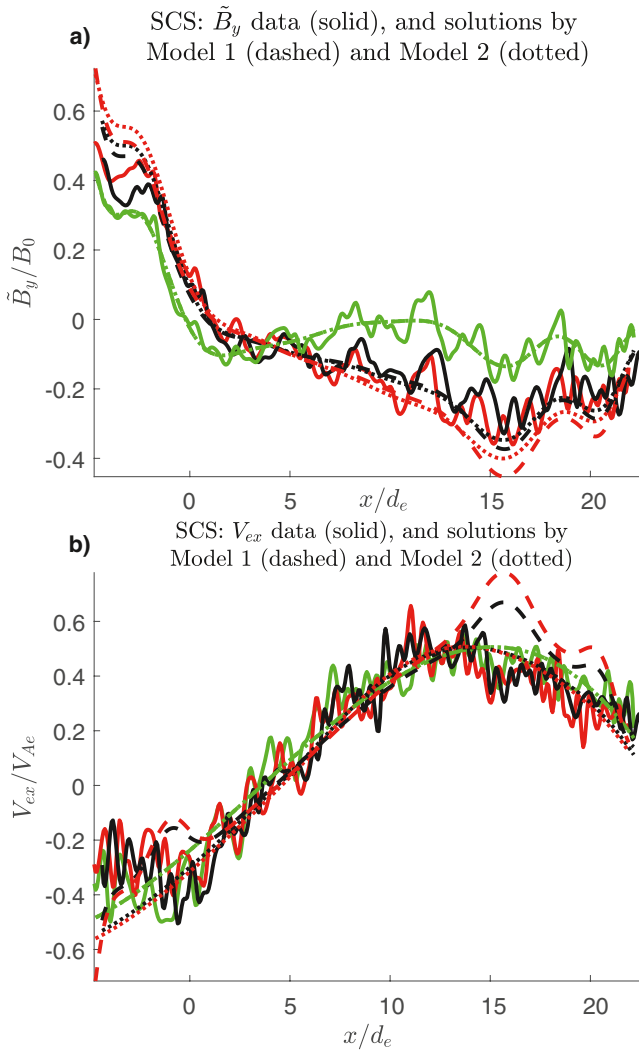
Figure 9. Reconstruction in SCS. Top: $\tilde{B}_y$, bottom: V_{ex}. Observed values (solid) as compared to the reconstruction prediction, evaluated by Equation 18 (dashed) and Equation 22 (dotted). The color code is the same to the one of Figure 2. BC: MMS3. For better visibility, reconstruction results for MMS4 are not shown.

4.2. Comparison of Model 2 with Model 3

In Model 3 magnetic potential is calculated by the same GSH Equation 17 as in Model 1. So, we need to compare the solutions for $\tilde{B}_y$ only. The mixed derivative in Equation 24 substantially complicates this equation, preventing using both BLA and the matrix method. Fortunately, Equation 24 has the form of the well-known Goursat problem (Goursat, 1915). With boundary conditions (for $\tilde{B}_y$) specified at the axes, this problem allows the unique solution in the rectangle $[0, x_0] \times [0, z_0]$ by means of the converging iterative procedure (Vladimirov, 1981). This procedure is applied as follows: the x axis is shifted at the MMS3 trajectory, and solution for $\tilde{B}_y$ is evaluated in each quadrant separately with the boundary conditions, specified at the x axis (MMS3 data) and at the z axis (solution, obtained from Model 2, demonstrating high accuracy at $x = 0$, as it is seen in Figures 7 and 9).

Since Equation 24 depends on the term ε, the Model 3 possesses some uncertainty. As it was mentioned in Section 2.1, in two-dimensional steady-state configuration $E_y = E_R$, where $E_R = const$ is the reconnection electric field, hence the value $\varepsilon = E_y/E_{Ae}$ is equal to $\sqrt{m_e / m_p} R_0$ under the proper choice of the normalization constants, where R_0 is the reconnection rate. Meanwhile, in the present study, the measured values of E_y demonstrate considerable oscillations and the offset of -1.8 mV/m at the MMS3 position (Figure 2a). This implies some freedom in the choice of the ε value. The series of reconstructions with varying ε revealed that the best reconstruction accuracy is obtained for $\varepsilon \in [0.062, 0.089]$, corresponding to reconnection electric field $E_R \in [2.8, 4.0]$ mV/m (see Figure 2a). The choice of a specific value within this interval is impeded by the fact that minimum value provides for the best accuracy of the $\tilde{B}_y$ reconstruction with very low accuracy for V_{ex}, the maximum value yields the higher accuracy of the V_{ex} reconstruction with the worse result for $\tilde{B}_y$. These features are demonstrated in Figure 11 and Figure 12, discussed below.

In Figure 11 the observed values of B_y, V_{ex} and V_{ez} are compared to the reconstruction prediction, evaluated by Equations 22 and 24 with included or omitted inertial term $\partial V_{ey}/\partial A$ and $E_R = 4$ mV/m. For the sake of a better visibility, the data of MMS1 and MMS4 and corresponding solutions are not shown. Figures 11a shows that in the most part of the CS all solutions show approximately the same good reconstruction quality. In more details, Model 2 benefits in the interval $-2 < x < 7$ and $x > 17$, Model 3 with omitted inertial term performs the best in $[7 < x < 17]$ and at $x < -2$; within the whole CS the inertial term contribution to the Model 3 reconstruction accuracy is either neutral or negative. Thus, in terms of the out-of-plane magnetic field reconstruction, neither Models 2 nor Model 3 demonstrate any evident advantage.

Figure 11b, where solutions for V_{ex} are shown, exhibits much more univocal results. At $x < -1$ Model 3 with omitted inertial term demonstrates good reconstruction accuracy, while the Model 2 fails. In the interval $-1 < x < 8$ both models provide a good accuracy. At $x > 8$ Model 2 shows the same high reconstruction accuracy, while solutions derived by Model 3 loose both qualitative and quantitative agreements with the MMS data. Note that Model 3 uses boundary conditions for $\tilde{B}_y$ only, the value of V_{ex} at the MMS3 trajectory is obtained from the solution of Equation 24. As concerns the inertial term, its contribution to V_{ex} solution accuracy is either neutral or negative again.

The solutions for V_{ez}, plotted in Figure 11c, demonstrate considerably worse results. Actually, both Model 2 and Model 3 with omitted inertial term reveal appropriate solutions in the small interval $0 < x < 5$ only.
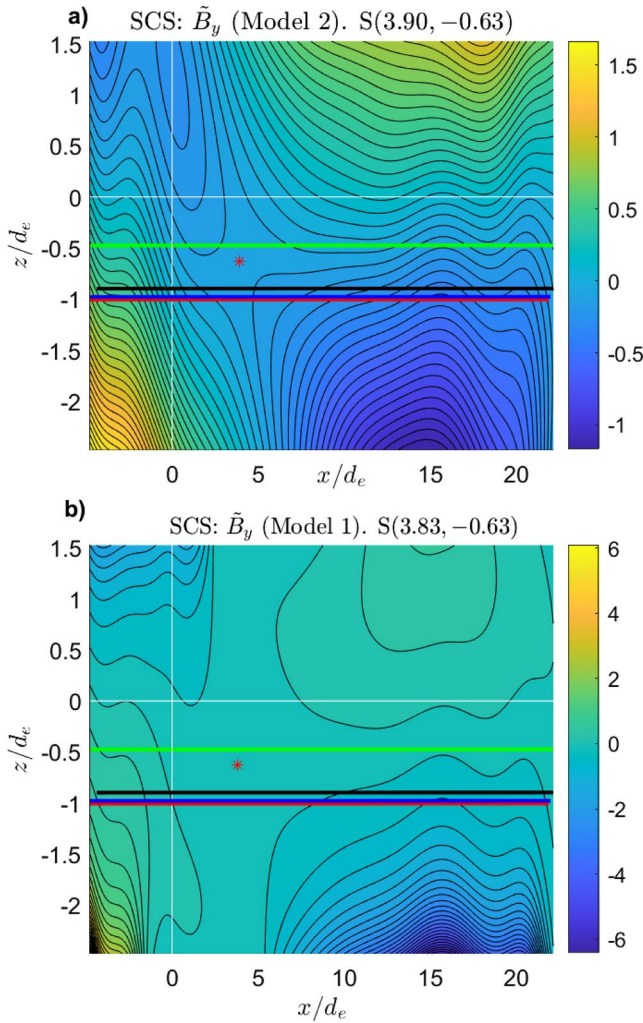
Figure 10. Reconstruction in SCS. Solutions for $\tilde{B}_y$ as obtained from Equation 22 (top) and from Equation 18 (bottom). In both panels red asterisks mark the electron in-plane flow stagnation points S (coordinates are given in the titles). White lines plot the axes, and horizontal colored lines plot the trajectories of MMS probes (color code is the same to the one of Figure 5).

Outside this interval both models fail to reproduce the MMS data. By keeping inertial term in Equation 24, the successful reconstruction interval is extended to the left in the region $x < 0$.

Figure 12 represents the same plots, with the value of $E_R = 2.8$ mV/m utilized by Model 3. In this figure we do not show the solutions of Equation 24 with kept inertial term, exhibiting the same features as in Figure 11. Instead we plot reconstruction results at the MMS1 position. The profiles of Figure 12a demonstrate high accuracy of the $\tilde{B}_y$ reconstruction obtained by both models in the whole reconstruction region. Particularly, Model 3 demonstrates some overestimate of $\tilde{B}_y$ in the interval $7 < x < 17$, while Model 2 shows the underestimate in $x \in (7, 22)$. Thus, Model 3 benefits in the intervals $x > 17$ and $x < -3$, in the rest part of the CS Models 2 and 3 are equally worth. However, Model 3 solution for V_{ex}, drawn in Figure 12b by dashed curves, exhibits a considerable accuracy decrease with respect to the corresponding results depicted in Figure 11b. As for the solutions for V_{ez}, in Figure 12c they are as bad as in Figure 11c. Notably, the stagnation point location is also affected considerably by the reconnection electric field value utilized in Model 3. For $E_R = 4.0$ mV/m the earthward shift of the stagnation point amounted to 92 km, while for $E_R = 2.8$ mV/m it has increased up to 140 km (in LMN').
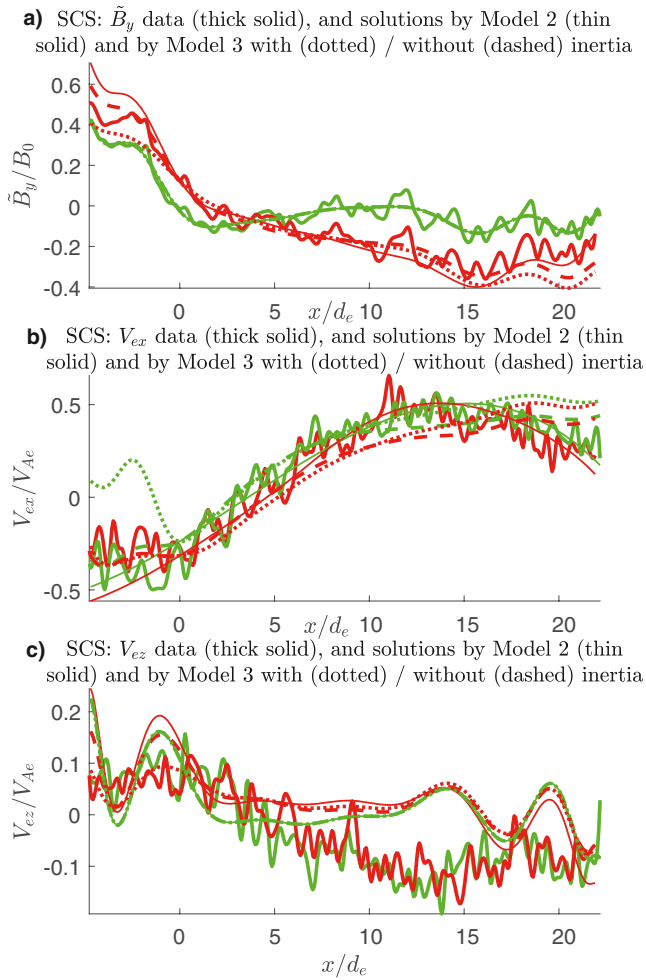
Summarizing the above, the comparison of Models 2 and 3 reveals that in terms of the B_y reconstruction they achieve a similar good accuracy. Under the proper choice of the reconnection electric field value, Model 3 may yield a more accurate solution. Particularly, this model yields unexpectedly good results in the region $x < 0$ (which is especially surprising in the interval $x < -3$, where reconstruction of B_x, plotted in Figure 7a, fails). However, in terms of the velocity V_{ex} reconstruction, Model 3 benefits at $x < 0$ only, in the rest part of the CS it fails rather fast (at $x \approx 8$ for $E_R = 4$ mV/m and at $x \approx 4$ for $E_R = 2.8$ mV/m). The inertial term in Equation 24 is found to be redundant since it is rather worsening the reconstruction accuracy than improving it (except for V_{ez}, which is actually not reconstructed properly neither by Model 2 nor by Model 3). Perhaps, it may be explained by the fact that the Hesse et al. (1999) approximation for $(\nabla \cdot \hat{P}_e)_y$ is obtained without taking this term into account. On average, Model 2 benefits over Model 3 because it provides more than two times bigger region of accurate V_{ex} reconstruction.

5. Discussion and Conclusions

In the present paper we considered the problem of reconstruction of the magnetic configuration in the electron diffusion region of magnetic reconnection. The problem is addressed in the frame of a steady-state two-dimensional model, in which we adopt the EMHD approximation $|\mathbf{j}_i| \ll |\mathbf{j}_e|$ and assume a uniform plasma density. The problem stated this way is reduced to the system of two equations, for scalar magnetic potential A of the in-plane magnetic field and for the out-of-plane magnetic field component B_y; the problem allows the coordinates transform $(x, z) \rightarrow (A, B_y)$.

The problem is considered by means of three different reconstruction models. Model 1 takes an assumption $V_{ey} = V_{ey}(A)$, leading to the system decouple to two independent Grad—Shafranov Equations 17 and 18. Model 2 assumes $V_{ey} = V_{ey}(A, B_y)$, resulting in two coupled Poisson's Equations 21 and 22. The right-hand sides of Equations 18 and 22 for B_y represent the contribution of the electron inertia to the equation of motion. Finally, Model 3 assumes $V_{ey} = V_{ey}(A)$, and equation for B_y (24) relies on the Hesse et al. (1999) approximation Equation 23 for the y component of the electron pressure tensor divergence, $(\nabla \cdot \hat{P}_e)_y$.

a) SCS: $\tilde{B}_y$ data (thick solid), and solutions by Model 2 (thin solid) and by Model 3 with (dotted) / without (dashed) inertia

b) SCS: V_{ex} data (thick solid), and solutions by Model 2 (thin solid) and by Model 3 with (dotted) / without (dashed) inertia

c) SCS: V_{ez} data (thick solid), and solutions by Model 2 (thin solid) and by Model 3 with (dotted) / without (dashed) inertia
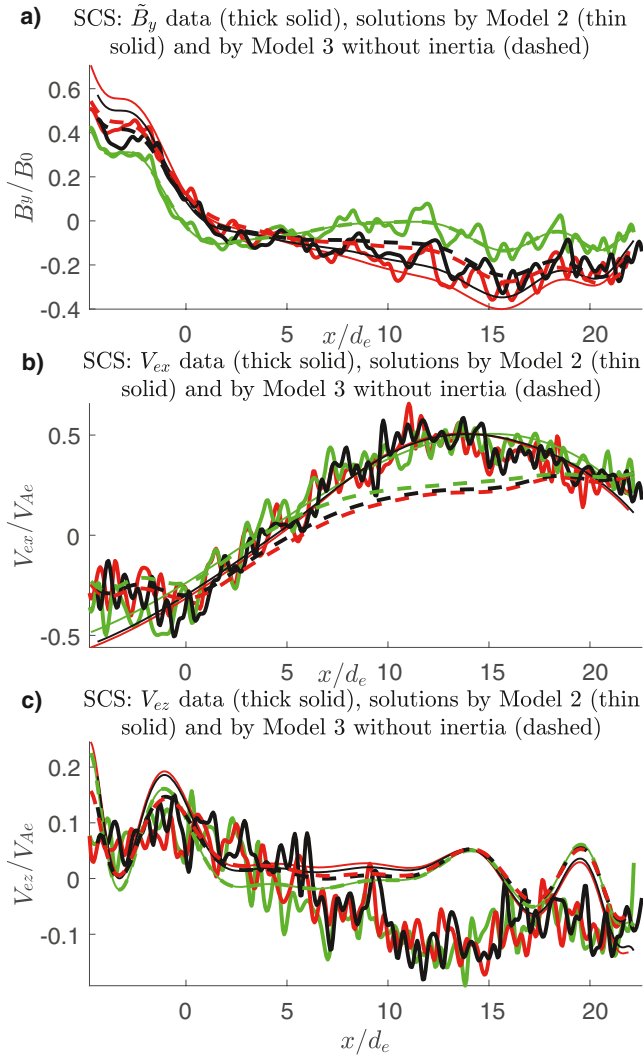
Figure 11. Reconstruction in SCS with $\varepsilon = 0.089$ (reconnection electric field $E_R = 4.0$ mV/m). Top: $\tilde{B}_y$, middle: V_{ex}, bottom: V_{ez}. Observed values (thick solid) as compared to the reconstruction prediction, evaluated by Equation 22 (thin solid) and by Equation 24 with kept (dotted) and omitted (dashed) inertial term. The color code is the same to the one of Figure 2. BC: MMS3. For better visibility, MMS1 and MMS4 data and corresponding reconstruction results are not shown.

We applied these three models to the EDR crossing event of July 11, 2017 reported by Torbert et al. (2018), when MMS spacecraft were located in the very close vicinity of the reconnection X-line for about 3 s. Profiles of the magnetoplasma quantities (Figure 2), registered by MMS probes, confirm that the CS conditions within this time period were mainly consistent with the model assumptions (except for the first 0.4 s and except for E_y offset at MMS3 position). Another important feature of this particular event is that it has being studied carefully in a number of works, including the paper of Hasegawa et al. (2019), where the reconstruction Model 3 has been successfully applied; so that the cited paper provided a convenient starting/reference point for our analysis. However, in our studies the reconstruction interval is increased from 1.4 to 3.22 s, starting from 22:34:01.70 UT.

The major difference of the three considered models consists in different approaches to B_y reconstruction. Particularly, Models 1 and 2 depend on the function $Q = \Delta_\perp B_y$, which value along the MMS trajectory is estimated by using Equation 1; this estimate is possible due to small spacing of the MMS probes (the maximum spacecraft separation did not exceed the value of 18 km, corresponding to 0.63 d_e in our normalization), exhibiting the regular tetrahedron constellation (see Figure 2 of Genestreti et al. (2018)). However, the functional dependence of this quantity is not defined. Therefore we considered two options: $Q = Q(\tilde{B}_y)$ in Model 1 and $Q = Q(A)$ in Model 2, where $\tilde{B}_y$ is the non-uniform part of the out-of-plane magnetic field. These two models provide self-consistent solutions of the system of EMHD equations under the assumptions $V_{ey} = V_{ey}(A)$ and $V_{ey} = V_{ey}(A, B_y)$, respectively. The comparison of the solutions for $\tilde{B}_y$ and V_{ex} (Figure 9) has demonstrated the benefit of Model 2 even at small distances of about 0.4 d_e (the distance between MMS3 and MMS1), as well as at larger distances. Solutions for magnetic potential and in-plane magnetic components (Figures 7 and 8) reveal that both models provide similar good accuracy. This can be explained by a small second term in the right-hand side of Equation 21. To arrive at the more univocal conclusion, one should use a data set with irregular MMS spacecraft configuration, where one probe is significantly remote; or instead the PIC-simulations data can be engaged. Grounding in the present results, we can conclude that V_{ey} is to be treated as two-dimensional function, since neglect of the B_y-dependence (even a weak one) results in inappropriate Equation 18 for B_y.

The solution by Model 2 occurs very supportive for addressing the Model 3. Namely, by using this solution in the capacity of the boundary conditions, Equation 24, considered as the Goursat problem, allows an exact solution (Vladimirov, 1981). The comparison of the solutions for $\tilde{B}_y$ and in-plane electron velocity, obtained in the frame of Model 2 and Model 3 reveals the following results: (a) in terms of $\tilde{B}_y$ reconstruction, both models perform nearly the same good; (b) in terms of V_{ex} reconstruction Model 3 shows much shorter applicability domain; (c) both models fail in V_{ez} reconstructing; (d) Model 3 benefits in the leftmost part of the CS at $x < 0$.

The lower accuracy of the Model 2 solution at $x < 0$ is presumably caused by the inaccuracy in the extrapolating function $Q(A)$. Looking in Figure 3g, one can see that on the left side the data become very uncertain. As for the failure of the V_{ez} reconstruction, it may have the more transparent physical reason. According to Equation 1, it may mean that in reality $\partial B_x/\partial y \neq 0$ (note that with the specified structure velocity $\mathbf{V}_0$, the length of the MMS trajectory in the y direction amounted for $\approx 3/4$ of the longitudinal path length). The inaccurate solution for V_{ex}, resulting from Model 3, is explained by inappropriate solution for V_{ez}, since this velocity component, multiplied by B_x, contributes to Equation 24. At the same time, the solution for $\tilde{B}_y$

a) SCS: $\tilde{B}_y$ data (thick solid), solutions by Model 2 (thin solid) and by Model 3 without inertia (dashed)

b) SCS: V_{ex} data (thick solid), solutions by Model 2 (thin solid) and by Model 3 without inertia (dashed)

c) SCS: V_{ez} data (thick solid), solutions by Model 2 (thin solid) and by Model 3 without inertia (dashed)

Figure 12. Reconstruction in SCS with $\varepsilon = 0.062$ (reconnection electric field $E_R = 2.8$ mV/m). Top: $\tilde{B}_y$, middle: V_{ex}, bottom: V_{ez}. Observed values (thick solid) as compared to the reconstruction prediction, evaluated by Equation 22 (thin solid) and by Equation 24 with omitted inertial term (dashed). The color code is the same to the one of Figure 2. BC: MMS3. For better visibility, MMS4 data and corresponding reconstruction results are not shown.

from Model 3 is completely specified by the boundary conditions for $\tilde{B}_y$, by constants ε and n, and by the solution for $A(x, z)$. Therefore, it is not affected by the inaccuracy of the solutions for velocity components. It is curious that Equation 24, resting upon a number of simplifying assumptions listed in Section 2.2, reveals the same B_y reconstruction accuracy (at least at small distances considered here) as Equation 22, derived from the exact Ohm's law. It may be explained by mutually exclusive effects of these assumptions.

Summarizing the above, the comparative study of three reconstruction models, formulated in Section 2.2, has shown that Model 1 is, in general, inappropriate, except for the case of very small values of the function Q, when both Equations 18 and 22 perform at small distances as the Laplace equation. In case of the real CS conditions, considered in this paper, where both stationarity and two-dimensionality are violated, Equation 24 of Model 3 appears appropriate for reconstructing B_y but not $\mathbf{V}_{e\perp}$. Model 2 is not affected so much by these violations (except for the solution for V_{ez}), demonstrating, on average, the best accuracy in the region of well-defined function $Q(A)$. The failure of V_{ez} reconstruction leads also to a low accuracy of the stagnation point location estimate.

The substantial advantage of Model 2 (and Model 1) is that it does not depend on the reconnection electric field, E_R, whose value imposes large uncertainty, because the measured values of E_y are strongly oscillating (see Figure 2a). For example, in the paper of Hasegawa et al. (2019), this electric field is estimated as $2-4$ mV/m. The analogous estimate by Genestreti et al. (2018) amounted to 3.2 ± 0.6 mV/m. Our estimate, based on the Model 3 reconstruction accuracy, is close to the latter one, amounting to $2.8-4.0$ mV/m.

The estimate of the basic assumptions, adopted in our analysis, namely, the CS steady-state and two-dimensionality, is given by the comparison of the reconnection electric field with the reconnection rate, R_0, which we evaluate by formula of Liu et al. (2017),

$$R_0 = \tan\phi \left(\frac{1 - \tan^2\phi}{1 + \tan^2\phi} \right) \sqrt{1 - \tan^2\phi}, \tag{25}$$

where 2ϕ is the separatrices opening angle. With the value of $2\phi = 22.5°$, obtained from the Model 2 solution, Equation 25 yields the reconnection rate $R_0 = 0.18$ (the analogous estimate in Hasegawa et al. (2019) amounted to 0.17, the difference is likely explained by the different sizes of the reconstruction regions). Recalculating reconnection electric field estimate $E_R = 2.8-4.0$ mV/m to the Hasegawa et al. (2019) normalization, using the global CS parameters ($E_A^H = 15.7$ mV/m), we derive the reconnection rate estimate $E_R / E_A^H = 0.18 - 0.25$. Thus, the value $R_0 = 0.18$, obtained by Equation 25, corresponds to the lowest estimate for $E_R = 2.8$ mV/m. This, in turn, is 10–20% higher than the average value of E_y, observed by MMS1, MMS2 and MMS4, amounting to {2.5, 2.6, 2.3} mV/m, respectively. This means that non-ideality of the CS conditions should produce the 10–20% inaccuracy of the reconstruction results. An error of that particular order is demonstrated by the solutions for the in-plane magnetic field components (see Figure 7).

Since Equation 21 of Model 2 depends on the term $\sim \tilde{B}_y$, implementation of this model requires the estimate of the guide field value, B_g, which has to be deduced from the measured value of B_y. Our study has shown that the requirement of the in-plane magnetic field vanishing at the X-point provides the condition that can be used for deriving the self-consistent estimate of B_g and local LMN coordinate system orientation.

The corresponding iterative procedure is realized in two steps. First, the choice of any particular value of B_g specifies the orientation of the coordinate system LMN_l by the requirement that in LMN_l both $\tilde{B}_M$ and B_N components change sign at the N axis, where $\tilde{B}_M = B_M - B_g$. With the requirement that B_L component changes sign at the L axis of LMN_l, this coordinate system is completely defined. Second, the values of the in-plane magnetic field components in the origin of coordinates, $B_L(0)$ and $B_N(0)$, are evaluated by reconstruction in LMN_l. Under the proper choice of B_g the origin of coordinates coincides with the X-point, hence $B_L(0) = B_N(0) = 0$. The estimate of $B_g = 0.45$ nT, obtained by means of this procedure, is consistent with the estimates of Genestreti et al. (2018) and Torbert et al. (2018). Implementation of this technique requires the satellite trajectory passing close to the X-line, where symmetry is not expected to be violated significantly. Besides that, the accuracy is restricted by the CS physical conditions, also restricting the accuracy of the magnetic potential reconstruction. This means that inaccuracy of the obtained estimate of B_g is about of 10%.

Apart from the general limitations of the analytical approach utilized in our study (which are discussed in (Korovinskiy et al., 2020)), such as steady-state CS, "infinite" X-line, and isotropic model for the in-plane electron pressure, the major limitation of Model 2 is related to derivation of Equation 22, based on Equation 20 for V_{ey}. The latter represents the Taylor series on $\tilde{B}_y$, where all terms except for two first ones are omitted under the assumption $|B_g| > |\tilde{B}_y|$. Looking at green dashed curve of Figure 4, we see that at the MMS3 trajectory this condition is fulfilled everywhere, except for the leftmost part of reconstruction interval, $t < 0.4$. However, in general, this condition may fail. Model 2 is easily modified for the case $B_g = 0$ by keeping quadratic term of the Taylor series instead of the linear one, but for the case $|B_g| \sim |\tilde{B}_y|$ this approach fails, since both linear and quadratic terms are to be kept, hence instead of the function $Q(A)$ we obtain two functions, $Q_1(A)$ and $Q_2(A)$, which cannot be distinguished in the boundary conditions data. Due to the same reason, we cannot address a more accurate estimate of Model 2 applicability condition, $\max|Q_1(A)\tilde{B}_y| > \max|Q_2(A)\tilde{B}_y^2|$. The estimate $|B_g| > |\tilde{B}_y|$ is rather rough: Figure 12a demonstrates the good reconstruction quality even in those regions, where $|\tilde{B}_y|$ exceeds the value of 0.15, which is the normalized guide field value B_g/B_0, up to three times. Thus, the only available estimate for the Model 2 applicability (in view of the B_g value) is $|\tilde{B}_y| < k|B_g|$ with the coefficient $k \sim 1$.

With Equations 12 and 13, Model 2 allows further generalization by replacing the condition $n_e = const$ by the less restrictive condition $n_e = n_e(A)$. According to results from our previous study (Korovinskiy et al., 2020), this might allow extending the reconstruction region in longitudinal direction up to the boundary of the EMHD domain. As concerns the cross-size of the reconstruction region, the problem is more complicated, since number density becomes the function of both variables, A and B_y, at very small distance from the x axis. PIC-simulations data analysis of Korovinskiy et al. (2020) revealed an estimate of $0.2\,d_p$ for this crucial distance (see Figure 10a, ibid). With the mass ratio $m_p/m_e = 256$ used in that study, it corresponds to the distance of $3\,d_e$. Notably, release of the condition $n_e = const$ would break one of the basic assumptions of Model 3. This means that aforementioned generalization of Model 2 could allow reconstruction of B_y in the region, where Model 3 is expected to fail.

Data Availability Statement

The MMS data used here are available from the MMS Science Data Center: https://lasp.colorado.edu/mms/sdc/public/.

References

Bhattacharjee, A. (2004). Impulsive magnetic reconnection in the earth's magnetotail and the solar corona. *Annual Review of Astronomy and Astrophysics*, *42*, 365–384. https://doi.org/10.1146/annurev.astro.42.053102.134039

Birn, J., Drake, J. F., Shay, M. A., Rogers, B. N., Denton, R. E., Hesse, M., et al. (2001). Geospace Environmental Modeling (GEM) magnetic reconnection challenge. *Journal of Geophysical Research*, *106*(A3), 3715–3719. https://doi.org/10.1029/1999JA900449

Biskamp, D. (2000). *Magnetic reconnection in plasmas*. Cambridge University Press. https://doi.org/10.1017/cbo9780511599958

Biskamp, D., Schwarz, E., & Drake, J. F. (1997). Two-fluid theory of collisionless magnetic reconnection. *Physics of Plasmas*, *4*(4), 1002–1009. https://doi.org/10.1063/1.872211

Bulanov, S. V., Pegoraro, F., & Sakharov, A. S. (1992). Magnetic reconnection in electron magnetohydrodynamics. *Physics of Fluids B*, *4*(8), 2499–2508. https://doi.org/10.1063/1.860467

Cassak, P. A., & Fuselier, S. A. (2016). Reconnection at earth's dayside magnetopause. In W. Gonzalez, & E. Parker (Eds.), *Magnetic reconnection: Concepts and applications* (Vol. 427, pp. 213–276). Springer. https://doi.org/10.1007/978-3-319-26432-5_6

Cassak, P. A., Liu, Y.-H., & Shay, M. A. (2017). A review of the 0.1 reconnection rate problem. *Journal of Plasma Physics*, *83*(5), 715830501. https://doi.org/10.1017/S0022377817000666

Comisso, L., & Bhattacharjee, A. (2016). On the value of the reconnection rate. *Journal of Plasma Physics*, *82*(6), 595820601. https://doi.org/10.1017/S002237781600101X

Daughton, W., Scudder, J., & Karimabadi, H. (2006). Fully kinetic simulations of undriven magnetic reconnection with open boundary conditions. *Physics of Plasmas*, *13*(7), 072101. https://doi.org/10.1063/1.2218817

Denton, R. E., Torbert, R. B., Hasegawa, H., Genestreti, K. J., Manuzzo, R., Belmont, G., et al. (2021). Two-dimensional velocity of the magnetic structure observed on July 11, 2017 by the magnetospheric multiscale spacecraft. *Journal of Geophysical Research Space Physics*, *126*(3), e2020JA028705. https://doi.org/10.1029/2020JA028705

Divin, A., Lapenta, G., Markidis, S., Semenov, V. S., Erkaev, N. V., Korovinskiy, D. B., & Biernat, H. K. (2012). Scaling of the inner electron diffusion region in collisionless magnetic reconnection. *Journal of Geophysical Research*, *117*(A6). https://doi.org/10.1029/2011JA017464

Divin, A., Semenov, V., Korovinskiy, D., Markidis, S., Deca, J., Olshevsky, V., & Lapenta, G. (2016). A new model for the electron pressure non-gyrotropy in the outer electron diffusion region. *Geophysical Research Letters*, *43*(20), 565–610. https://doi.org/10.1002/2016GL070763

Dorfman, S., Ji, H., Yamada, M., Yoo, J., Lawrence, E., Myers, C., & Tharp, T. D. (2013). Three-dimensional, impulsive magnetic reconnection in a laboratory plasma. *Geophysical Research Letters*, *40*(2), 233–238. https://doi.org/10.1029/2012GL054574

Drake, J. F., Shay, M. A., & Swisdak, M. (2008). The Hall fields and fast magnetic reconnection. *Physics of Plasmas*, *15*(4), 042306. https://doi.org/10.1063/1.2901194

Egedal, J., Ng, J., Le, A., Daughton, W., Wetherton, B., Dorelli, J., et al. (2019). Pressure Tensor Elements Breaking the Frozen-In Law During Reconnection in Earth's Magnetotail. *Physical Review Letters*, *123*(22), 225101. https://doi.org/10.1103/PhysRevLett.123.225101

Frank, A. G. (1999). Magnetic reconnection and current sheet formation in 3D magnetic configurations. *Plasma Physics and Controlled Fusion*, *41*(3A), A687–A697. https://doi.org/10.1088/0741-3335/41/3A/062

Genestreti, K. J., Nakamura, T. K. M., Nakamura, R., Denton, R. E., Torbert, R. B., Burch, J. L., et al. (2018). How accurately can we measure the reconnection rate E M for the MMS diffusion region event of July 11, 2017? *Journal of Geophysical R*.

Gonzalez, W., & Parker, E. (2016). *Magnetic Reconnection* (Vol. 427). Springer. https://doi.org/10.1007/978-3-319-26432-5

Gosling, J. T., Asbridge, J. R., Bame, S. J., Feldman, W. C., Paschmann, G., Sckopke, N., & Russell, C. T. (1982). Evidence for quasi-stationary reconnection at the dayside magnetopause. *Journal of Geophysical Research*, *87*(A4), 2147–2158. https://doi.org/10.1029/JA087iA04p02147

Goursat, É. (1915). *Cours D'analyze Mathèmatique* (Vol. 3). Gauthier-Villars et Cie.

Grad, H., & Rubin, H. (1958). Hydromagnetic equilibria and force-free fields. *Journal of Nuclear Energy*, *7*(3–4), 284–285. https://doi.org/10.1016/0891-3919(58)90139-6

Hadamard, J. (1923). *Lectures on cauchy's problem in linear partial differential equations*. New Haven Yale University Press.

Hasegawa, H., Denton, R. E., Nakamura, R., Genestreti, K. J., Nakamura, T. K. M., Hwang, K. J., et al. (2019). Reconstruction of the electron diffusion region of magnetotail reconnection seen by the MMS spacecraft on July 11, 2017. *Journal of Geophysical Research Space Physics*, *124*(1), 122–138. https://doi.org/10.1029/2018JA026051

Hasegawa, H., Sonnerup, B. U. Ö., Denton, R. E., Phan, T.-D., Nakamura, T. K. M., Giles, B. L., et al. (2017). Reconstruction of the electron diffusion region observed by the Magnetospheric Multiscale spacecraft: First results. *Geophysical Research Letters*, *44*(10), 4566–4574. https://doi.org/10.1002/2017GL073163

Hesse, M., & Cassak, P. A. (2020). Magnetic reconnection in the space sciences: past, present, and future. *Journal of Geophysical Research Space Physics*, *125*(2), e25935. https://doi.org/10.1029/2018JA025935

Hesse, M., Neukirch, T., Schindler, K., Kuznetsova, M., & Zenitani, S. (2011). The diffusion region in collisionless magnetic reconnection. *Space Science Reviews*, *160*(1–4), 3–23. https://doi.org/10.1007/s11214-010-9740-110.1007/978-1-4614-3046-9_2

Hesse, M., Schindler, K., Birn, J., & Kuznetsova, M. (1999). The diffusion region in collisionless magnetic reconnection. *Physics of Plasmas*, *6*(5), 1781–1795. https://doi.org/10.1063/1.873436

Hesse, M., & Winske, D. (1998). Electron dissipation in collisionless magnetic reconnection. *Journal of Geophysical Research*, *103*(A11), 26479–26486. https://doi.org/10.1029/98JA01570

Ji, X.-F., Wang, X.-G., Sun, W.-J., Xiao, C.-J., Shi, Q.-Q., Liu, J., & Pu, Z.-Y. (2014). EMHD theory and observations of electron solitary waves in magnetotail plasmas. *Journal of Geophysical Research Space Physics*, *119*(6), 4281–4289. https://doi.org/10.1002/2014JA019924

Karimabadi, H., Daughton, W., & Scudder, J. (2007). Multi-scale structure of the electron diffusion region. *Geophysical Research Letters*, *34*(13). https://doi.org/10.1029/2007GL030306

Korovinskiy, D. B., Divin, A. V., Semenov, V. S., Erkaev, N. V., Kiehas, S. A., & Kubyshkin, I. V. (2020). Grad-Shafranov reconstruction of the magnetic configuration in the reconnection X-point vicinity in compressible plasma. *Physics of Plasmas*, *27*(8), 082905. https://doi.org/10.1063/5.0015240

Korovinskiy, D. B., Semenov, V. S., Erkaev, N. V., Divin, A. V., & Biernat, H. K. (2008). The 2.5-D analytical model of steady-state Hall magnetic reconnection. *Journal of Geophysical Research*, *113*(A4). https://doi.org/10.1029/2007JA012852

Korovinskiy, D. B., Semenov, V. S., Erkaev, N. V., Divin, A. V., Biernat, H. K., & Möstl, U. V. (2011). A 2.5-D electron Hall-MHD analytical model of steady state Hall magnetic reconnection in a compressible plasma. *Journal of Geophysical Research*, *116*(A5), A05219. https://doi.org/10.1029/2010JA015942

Kuznetsova, M. M., Hesse, M., Rastätter, L., Taktakishvili, A., Toth, G., De Zeeuw, D. L., et al. (2007). Multiscale modeling of magnetospheric reconnection. *Journal of Geophysical Research*, *112*(A10). https://doi.org/10.1029/2007JA012316

Kuznetsova, M. M., Hesse, M., & Winske, D. (1998). Kinetic quasi-viscous and bulk flow inertia effects in collisionless magnetotail reconnection. *Journal of Geophysical Research*, *103*(A1), 199–213. https://doi.org/10.1029/97JA02699

Kuznetsova, M. M., Hesse, M., & Winske, D. (2000). Toward a transport model of collisionless magnetic reconnection. *Journal of Geophysical Research*, *105*(A4), 7601–7616. https://doi.org/10.1029/1999JA900396

Li, T. C., Liu, Y. H., Hesse, M., & Zou, Y. (2020). Three-Dimensional X-line Spreading in Asymmetric Magnetic Reconnection. *Journal of Geophysical Research Space Physics*, *125*(2), e27094. https://doi.org/10.1029/2019JA027094

Liu, Y.-H., Hesse, M., Guo, F., Daughton, W., Li, H., Cassak, P. A., & Shay, M. A. (2017). Why does steady-state magnetic reconnection have a maximum local rate of order 0.1? *Physical Review Letters*, *118*(8), 085101. https://doi.org/10.1103/PhysRevLett.118.085101

Nakamura, R., Genestreti, K. J., Nakamura, T., Baumjohann, W., Varsani, A., Nagai, T., et al. (2019). Structure of the current sheet in the 11 July 2017 electron diffusion region event. *Journal of Geophysical Research Space Physics*, *124*(2), 1173–1186. https://doi.org/10.1029/2018JA026028

Øieroset, M., Phan, T. D., Fujimoto, M., Lin, R. P., & Lepping, R. P. (2001). In situ detection of collisionless reconnection in the Earth's magnetotail. *Nature*, *412*(6845), 414–417. https://doi.org/10.1038/35086520

Paschmann, G., Øieroset, M., & Phan, T. (2013). In-situ observations of reconnection in space. *Space Science Reviews*, *178*(2–4), 385–417. https://doi.org/10.1007/s11214-012-9957-2

Phan, T. D., Dunlop, M. W., Paschmann, G., Klecker, B., Bosqued, J. M., Rème, H., et al. (2004). Cluster observations of continuous reconnection at the magnetopause under steady interplanetary magnetic field conditions. *Annales Geophysicae*, *22*(7), 2355–2367. https://doi.org/10.5194/angeo-22-2355-2004

Retinò, A., Bavassano Cattaneo, M. B., Marcucci, M. F., Vaivads, A., André, M., Khotyaintsev, Y., et al. (2005). Cluster multispacecraft observations at the high-latitude duskside magnetopause: Implications for continuous and component magnetic reconnection. *Annales Geophysicae*, *23*(2), 461–473. https://doi.org/10.5194/angeo-23-461-2005

Schindler, K. (2007). *Physics of space plasma activity*. Cambridge University Press.

Scudder, J. D. (2016). Collisionless reconnection and electron demagnetization. In W. Gonzalez, & E. Parker (Eds.), *Magnetic reconnection: Concepts and applications* (Vol. 427, pp. 33–100). Springer. https://doi.org/10.1007/978-3-319-26432-5_210.1007/978-3-319-26432-5_2

Semenov, V., Korovinskiy, D., Divin, A., Erkaev, N., & Biernat, H. (2009). Collisionless magnetic reconnection: analytical model and PIC simulation comparison. *Annales Geophysicae*, *27*(3), 905–911. https://doi.org/10.5194/angeo-27-905-2009

Shafranov, V. (1966). Plasma equilibrium in a magnetic field. *Reviews of plasma physics*, *2*, 103.

Shay, M. A., Drake, J. F., & Swisdak, M. (2007). Two-scale structure of the electron dissipation region during collisionless magnetic reconnection. *Physical Review Letters*, *99*(15), 155002. https://doi.org/10.1103/PhysRevLett.99.155002

Sonnerup, B. U. Ö. (1979). Magnetic field reconnection. Solar Sys. *Plasma Physics*, *3*, 45–108.

Sonnerup, B. U. Ö., Hasegawa, H., Denton, R. E., & Nakamura, T. K. M. (2016). Reconstruction of the electron diffusion region. *Journal of Geophysical Research Space Physics*, *121*(5), 4279–4290. https://doi.org/10.1002/2016JA022430

Torbert, R. B., Burch, J. L., Phan, T. D., Hesse, M., Argall, M. R., Shuster, J., et al. (2018). Electron-scale dynamics of the diffusion region during symmetric magnetic reconnection in space. *Science*, *362*(6421), 1391–1395. https://doi.org/10.1126/science.aat2998

Uzdensky, D. A., & Kulsrud, R. M. (2006). Physical origin of the quadrupole out-of-plane magnetic field in Hall-magnetohydrodynamic reconnection. *Physics of Plasmas*, *13*(6), 062305. https://doi.org/10.1063/1.2209627

Vladimirov, V. S. (1981). *Equations of mathematical physics* (pp. 247–252). Nauka. (in Russian).

Xiao, C. J., Wang, X. G., Pu, Z. Y., Zhao, H., Wang, J. X., Ma, Z. W., et al. (2006). In situ evidence for the structure of the magnetic null in a 3D reconnection event in the Earth's magnetotail. *Nature Physics*, *2*(7), 478–483. https://doi.org/10.1038/nphys342

Yamada, M., Kulsrud, R., & Ji, H. (2010). Magnetic reconnection. *Reviews of Modern Physics*, *82*(1), 603–664. https://doi.org/10.1103/RevModPhys.82.603